

Platinum-Decorated Gold Nanoparticle-Based Microfluidic Chip Immunoassay for Ultrasensitive Colorimetric Detection of SARS-CoV-2 Nucleocapsid Protein

Feng Wu, Mao Mao, Liangyu Cai, Qianyu Lin, Xuejiao Guan, Xueying Shi, and Lan Ma*

Cite This: <https://doi.org/10.1021/acsbomaterials.2c00600>

Read Online

ACCESS |



Metrics & More



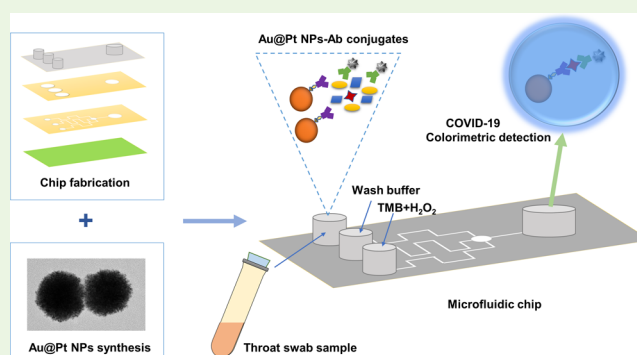
Article Recommendations



Supporting Information

ABSTRACT: Gold nanoparticle-based point-of-care tests (POCT) are one of the most widely used diagnostic tools for SARS-CoV-2 screening. However, the limitation of their insufficient sensitivity often leads to false negative results in early disease diagnostics. The ongoing pandemic of COVID-19 makes diagnostic tools that are more accurate, sensitive, simple, and affordable in high demand. In this work, we develop a platinum-decorated gold nanoparticle (Au@Pt NP)-based microfluidic chip immunoassay with a sensitivity surpassing that of paper-based detection of nucleocapsid (N) protein, one of the most conserved biomarkers of COVID-19. The synthesized Au@Pt NPs show high stability and catalytic activity in complex environments. The catalytic amplification of Au@Pt NPs enables naked-eye detection of N protein in the low femtogram range (ca. 0.1 pg/mL) and the detection of throat swab samples in under 40 min. This microfluidic chip immunoassay is easy for operation and readout without instrument assistance, making it more suitable for on-site detection and future pathogen surveillance.

KEYWORDS: COVID-19, nucleocapsid protein, microfluidic, immunoassay, nanoparticle



INTRODUCTION

Coronavirus disease 2019 (COVID-19) has developed into a global pandemic, and the variants of the virus reduce the protective efficacy of the vaccine, especially the omicron variant, which shows a more contagious nature and leads to an unprecedented level of disease transmission all over the world.¹ Due to the long incubation period of the SARS-CoV-2 virus, early and large-scale screening of COVID-19 is critical for successful control of the pandemic. Since the beginning of this pandemic, researchers have developed different methods for detecting SARS-CoV-2 virus such as CRISPR and SARSeq.^{2–4} The most commonly used detection methods are PCR-based viral nucleic acid detection, human serum antibody detection, and viral specific antigen detection, among which the PCR-based viral nucleic acid detection by RT-PCR is currently the gold standard for SARS-CoV-2 detection due to its high accuracy of directly detecting the viral genome.^{5,6} However, the RT-PCR-based detection method can only operate in laboratory conditions equipped with professional equipment and needs highly trained operators due to the complicated operation of the nucleic acid extraction and amplification and also safety reasons. Thus, only a limited number of tests can be carried out each day, which makes it difficult to meet large-scale screening needs. The human serum antibody-based rapid test in the early COVID-19 pandemic was an effective strategy

for the diagnosis of SARS-CoV-2 infection but could not distinguish between the course of the infection and vaccination. Viral antigen detection by immunoassays is an alternative to RT-PCR-based detection approaches due to many advantages. Lateral flow assays (LFAs) for the detection of SARS-CoV-2 immunogenic proteins are the most used because of their rapid, low-cost, point-of-care (POC) characteristics. Most LFAs utilize nucleocapsid protein, which is the most conserved biomarker and only has a few mutational changes, and use nanomaterials such as colloidal gold, latex, quantum dots, and fluorescent microspheres as detection markers.^{7,8} With LFAs as the most prominent rapid POC tests of SARS-CoV-2, their sensitivity is generally lower than that of nucleic acid detection methods.⁹

The ongoing pandemic of COVID-19 needs diagnostic tools that are more accurate, sensitive, simple, and affordable. To increase the detection accuracy and sensitivity, new methods

Received: May 22, 2022

Accepted: July 25, 2022

are being developed, including signal amplification, electrochemical sensors, chemiluminescent sensors, microfluidic immunosensors, and graphene-based biosensors.^{10–22} In these immunosensors, antibodies or aptamers are pretreated with a signal amplification material, which captures target antigens and requires a long incubation time or requires specific equipment for result readout. Noble metal nanoparticles have high catalytic efficiency, high stability in complex environments, and easy production, which make them promising for signal amplification in colorimetric immunoassays and can significantly improve the sensitivity of ELISAs and LFAs.^{23–27} The peroxidase mimics with ultrahigh catalytic activities can quickly generate blue molecules by catalyzing the oxidation of 3,3',5,5'-tetramethylbenzidine (TMB) with H₂O₂ in aqueous solution. This catalytic reaction is cost-effective and nontoxic, and the test result can be easily judged with the naked eyes. However, the peroxidase mimic-based ELISA requires a long incubation time, and the limited structure of peroxidase mimic-based LFAs requires additional operation steps, which limit their large-scale application.^{23–25} Herein, we integrate peroxidase mimic Au@Pt NPs into a microfluidic immunoassay chip for rapid and sensitive analysis of SARS-CoV-2 N proteins. Through the design of the microfluidic architecture and optimization of the nanocatalyst amplification operation, we have obtained ultrahigh sensitivity and a simple operation process. Here, we show the naked-eye detection with a high sensitivity of femtogram concentrations of SARS-CoV-2 N protein (ca. 0.1 pg/mL) in under 40 min.

EXPERIMENTAL SECTION

Materials. Gold(III) chloride tetrahydrate (HAuCl₄·4H₂O, Au > 47.8%) was purchased from Beijing Huawei Ruike Chemical (Beijing, China). Hydrogen hexachloroplatinate(IV) hexahydrate (H₂PtCl₆·6H₂O, 99%) was purchased from Energy Chemicals (Shanghai, China). Polyvinylpyrrolidone (PVP, MW of 10,000) was purchased from Tokyo Chemical Industry. Streptavidin, sulfo-NHS-LC-biotin, 1-ethyl-3-[3-dimethylaminopropyl] carbodiimide hydrochloride (EDC), and *N*-hydroxysulfosuccinimide (sulfo-NHS) were purchased from Thermo Fisher Scientific (USA). Sodium citrate tribasic dihydrate (99%), L-ascorbic acid (AA, 99%), bovine serum albumin (BSA), and casein block were purchased from Sigma-Aldrich. A photoresist (SU-82050) was purchased from MicroChem Corp. (MA, USA). Polydimethylsiloxane (PDMS) (Sylgard 184) was purchased from Dow Corning (USA). 2-(*N*-Morpholino)ethanesulfonic acid (MES), disodium hydrogen phosphate (Na₂HPO₄, ≥99.0%), sodium phosphate monobasic monohydrate (NaH₂PO₄·H₂O, 98–102.0%), *N*-acetyl-L-cysteine (LNAC, 98.5–101.0%), Tween 20, and Nonidet (R) P-40 (NP40) were purchased from Sangon Biotech (Shanghai, China). 3,3',5,5'-Tetramethylbenzidine (TMB, >99%), a one-step TMB substrate solution, were purchased from Beijing Make-wonderbio (Beijing, China). Carboxyl-functionalized magnetic beads (MBs) with an average diameter of 10 μm were purchased from Suzhou Nanomicr Technology (China). SARS-CoV-2 nucleocapsid protein was purchased from Genscript Biotech Corporation. Mouse anti-SARS-CoV-2 nucleocapsid (N) protein antibodies (mAb IgG) were obtained from the Institute of Biopharmaceutical and Health Engineering, Tsinghua University. All aqueous solutions were prepared using deionized (DI) water produced by a Milli-Q Integral 10 system (18.2 MΩ·cm, Merck Millipore).

Fabrication of Gold Nanoparticles and Au@Pt NPs. Gold nanoparticles (Au NPs) were synthesized by classical sodium citrate reduction of HAuCl₄ with minor modifications.²⁸ Briefly, 600 mL of HAuCl₄ aqueous solution (1 mM) was added to a 1000 mL three-neck round-bottom flask equipped with a condenser and quickly heated to 100 °C under magnetic stirring. Then, the temperature was reduced to 70 °C, and 10 mL of sodium citrate tribasic dihydrate

aqueous solution (6%, w/v) was quickly added using a pipette. The mixture was kept stirring and refluxed for 30 min after its color turned to red. The synthesized Au NPs were cooled and stored at 4 °C for future use. The Au NP concentration (ca. 11 nM) was measured by TEM and initial gold concentration analysis.

Au@Pt NPs were synthesized by reducing chloroplatinic acid hydrate on gold seeds as adapted from Loynachan et al.²⁴ Briefly, 16 mL (11 nM) of Au NP seeds was added to 190 mL of deionized water; then, 4 mL of poly(vinylpyrrolidone) (PVP, MW of 10 kDa) (20%, w/v) was added and mixed strongly for 2 min for the polymer coating and stabilizing of the Au NP seeds. Thereafter, 8 mL of L-ascorbic acid (10%, w/v) was added to the mixture and mixed for 1 min. Chloroplatinic acid hydrate (1600 μL, 0.5 M) was then added to the mixture and mixed for 1 min. The solution was immediately heated to 65 °C in an oil bath with static conditions for 30 min until its color turned to brown/black. The synthesized Au@Pt NPs were cooled to room temperature and purified by centrifugation (15 min, 14,000g) and resuspended in deionized water three times. The Au@Pt NP size in the range of 35–125 nm was controlled by changing the added amount of Au NP seeds while keeping the addition of PVP, L-ascorbic acid, and H₂PtCl₆ constant.

Preparation of Au@Pt NPs–Antibody Conjugates. In this case, the antibody can form coordination bonds with the surface of Au@Pt NPs through sulfur groups. Briefly, 10 mg of DTT per milliliter of water was dissolved, and then, 25 μL of this solution was added per mg of mouse anti-SARS-CoV-2 N protein labeling antibodies (L-mAbs). The solution was mixed and reacted at 4 °C for 30 min. Excess DTT was removed by ultrafiltration centrifugation using 20 mM sodium phosphate buffer (containing 0.15 M NaCl and 1 mM EDTA, pH 7.4). The modified L-mAbs should be used immediately in a conjugation reaction. Then, 100 μL of 75 nm Au@Pt NPs (2.5 nM) was mixed with 400 μL of 20 mM sodium phosphate buffer followed by addition of 54 μg of modified L-mAbs. The mixture was incubated for 2 h using gentle rotation at room temperature. Conjugated Au@Pt NPs were subsequently blocked by adding 200 μL of blocking solution (containing 1 wt % casein block and 1 wt % glutathione in 20 mM phosphate buffer, pH 7.4) for 30 min using gentle rotation at room temperature. The Au@Pt NPs–antibody conjugates were purified by centrifugation (15 min, 14,000g) three times using 20 mM sodium phosphate buffer (containing 0.1 wt % casein block, 0.15 M NaCl, and 0.05 wt % Tween 20, pH 7.4). Au@Pt NPs–mAbs were finally resuspended in storage buffer at a concentration of 500 pM (containing 5 wt % sucrose, 1 wt % BSA, 0.5 wt % PVP (10 kDa), 0.1 wt % casein block, and 0.05 wt % Tween 20 in 20 mM phosphate buffer, pH 7.4).

Preparation of Magnetic Bead–Antibody Conjugates. Magnetic beads (MBs) and antibody conjugates were prepared according to the streptavidin–biotin systems. First, biotinylation of mouse anti-SARS-CoV-2 N protein coating antibodies (C-mAbs) was prepared. Briefly, C-mAbs were dialyzed against PBS and diluted to 2 mg/mL. Sulfo-NHS-LC-biotin was dissolved in DMSO at a concentration of 10 mM, and 13.5 μL of this solution was added to 500 μL of the C-mAbs solution and reacted for 24 h at 4 °C. The unreacted biotinylation reagent and reaction byproducts were removed by dialysis against PBS for 24 h at 4 °C. Streptavidin-conjugated MBs were prepared according to the EDC/NHS method. Carboxyl-functionalized MBs (10 mg) were separated with a magnet for 1 min and washed with 10 mM MES buffer three times, and then, 2 mM sulfo-NHS and 5 mM EDC were added to MBs and incubated for 30 min at 37 °C using gentle rotation. The activated MBs were separated with a magnet and washed three times and then redispersed in 50 mM borate buffer to react with 0.15 mg of streptavidin for 3 h at 37 °C using gentle rotation. Residual active coupling sites were blocked by addition of 200 μL of blocking solution (containing 5 wt % BSA and 1 wt % casein block in 20 mM phosphate buffer, pH 7.4) for 30 min at 37 °C. The streptavidin-coated MBs were washed four times using 20 mM sodium phosphate buffer (containing 0.15 M NaCl, 0.1 wt % casein block, and 0.1 wt % Tween 20, pH 7.4). The streptavidin-coated MBs and 0.3 mg of biotinylated antibodies in PBS were incubated for 1 h at room temperature using gentle rotation. The

antibody-coated MBs were separated with a magnet and washed four times using 20 mM sodium phosphate buffer (containing 0.15 M NaCl, 0.1 wt % casein block, and 0.1 wt % Tween 20, pH 7.4). Finally, MBs-streptavidin-mAbs were resuspended in 20 mM phosphate storage buffer (containing 5 wt % sucrose, 1 wt % bovine serum albumin, 0.5 wt % PVP (10 kDa), 0.1 wt % casein block, and 0.1 wt % Tween 20, pH 7.4).

Characterization Methods and Evaluations of the Au@Pt NP Activity. The surface topography of nanoparticles was acquired by transmission electron microscopy (TEM, F30, FEI, Hillsboro, OR, USA). High-resolution TEM images and energy-dispersive X-ray (EDS) mapping images of nanoparticles were acquired by field-emission transmission electron microscopy (JEM-3200FS, JEOL, Japan). The hydrodynamic size of nanoparticles was performed by dynamic light scattering (DLS) using a Zetasizer (Nano ZS90, Malvern Instruments, UK). XPS was measured with a PHI 5000 Versa Probe II spectrometer (Ulvac-Phi, Japan). Optical absorbance measurements were performed with a UV-vis spectrophotometer (Ultrospec 2100 pro, Amersham Biosciences, USA). Absorbances at 630 nm were measured using a microplate reader (ELX800, BioTek Instruments, USA).

All assays of activity evaluation were done at room temperature in a 96-well microplate. For stability and activity tests of Au@Pt NPs in acidic-to-alkaline pH environments, 10 μL of Au@Pt NPs (2.5 nM) was mixed with 990 μL of deionized water with different pHs for up to 30 min and 24 h at room temperature. For storage stability and activity of Au@Pt NPs in different temperature environments, 10 μL of Au@Pt NPs (2.5 nM) was mixed with 990 μL of purified water and stored in a 4 $^{\circ}\text{C}$ refrigerator, at room temperature (RT), and in a 37 $^{\circ}\text{C}$ incubator up to 5 weeks. Clinical matrices are also a particular concern for actual SARS-CoV-2 testing. The catalytic activity of the particles decreases due to the adsorption of proteins to Au@Pt NPs, we evaluated the catalytic activity of Au@Pt NPs-mAbs conjugates in different biosample, and 10 μL of Au@Pt NPs-mAbs (500 pM) conjugates was mixed with 90 μL of PBS, fetal bovine serum, saliva sample (100 μL of saliva mixed with 900 μL of PBS), and urine for up to 30 min and 24 h at room temperature. For catalytic activity tests, Au@Pt NPs were diluted in deionized water to 2.5 pM, while Au@Pt NPs-mAbs were diluted in PBS to 5 pM. During the activity test, 50 μL of Au@Pt NPs was added to a 96-well microplate followed by addition of 100 μL of TMB substrate solution. The reaction solution was measured at 630 nm absorbance using a microplate reader.

Peroxidase-like catalytic efficiencies of Au@Pt NPs were performed by steady-state kinetic assays.^{25,29} Briefly, all assays were done in a cuvette (path length, $l = 1.0$ cm) at room temperature by using 0.2 M NaOAc/HOAc buffer with pH 4.0 containing 1.0 M H_2O_2 . After addition of 5.0×10^{-13} M Au@Pt NPs and TMB with different concentrations, the absorbance at $\lambda_{\text{max}} = 653$ nm was detected by a UV-vis spectrophotometer using enzyme kinetic procedures with an interval of 2 s for 1 min. The slope at the initial point ($\text{Slope}_{\text{initial}}$) was obtained, and the initial reaction velocity (ν) was calculated from the equation $\nu = \text{Slope}_{\text{initial}} / (\epsilon_{\text{TMB-653nm}} \times l)$, where $\epsilon_{\text{TMB-653nm}}$ is the molar extinction coefficient of oxTMB at 653 nm ($39,000 \text{ M}^{-1} \cdot \text{cm}^{-1}$). The plots of ν against TMB concentrations were obtained by nonlinear regression of the Michaelis-Menten function in Origin 2022. The values of K_m and V_{max} were obtained from the double reciprocal plots, and the catalytic constant (K_{cat}) was obtained from the equation $K_{\text{cat}} = V_{\text{max}} / [E]$, where $[E]$ is the particle concentration of Au@Pt NPs.

Preparation of Microfluidic Chips and Test Procedures. The microfluidic chips were designed with AutoCAD 2019. The chips consist of four layers, including two PDMS layers, a 3D printed PMMA layer, and a PET film layer (Figure 1a). The 3D printed PMMA layer has three luer inlet ports and one luer outlet port. The inlets and outlets are connected to the chamber with channels of 1000 μm width. A height of 100 μm was considered for the chamber. The microchannel structure (Figure 1b) was fabricated in PDMS by rapid prototyping and replication processes as described elsewhere.³⁰ PDMS membranes and PDMS microchannels were prepared and cut with a certain shape. After the inlet and outlet holes were punched, the PDMS membranes were first bonded with the 3D

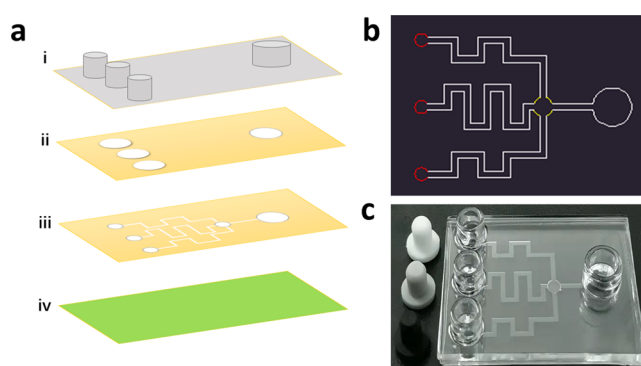


Figure 1. Schematic illustration of the microfluidic chips. (a) Schematic design of the microfluidic chip, (i) 3D printed PMMA layer, (ii) PDMS membrane layer, (iii) PDMS microchannel layer, and (iv) PET film layer. (b) AutoCAD layout of the structure in the microchannel. (c) Photograph of the microfluidic chip and the T-type silicone rubber plug.

printed PMMA layers by chemical bonding with a silane coupling agent. Then, the PDMS membrane and the PDMS microchannel with the nonchannel surface were exposed to oxygen plasma for 1 min and bonded to one another. After that the PDMS microchannel with the channel surface and the PET film were exposed to oxygen plasma for 1 min and bonded to one another. The chips were then baked in an oven at 80 $^{\circ}\text{C}$ for 1 h to strengthen the bonding. The prepared microfluidic chip is shown in Figure 1c.

For microfluidic chip immunoassay preparation, 10 μL of either Au@Pt NPs-mAbs conjugates (500 pM) or MB-mAbs conjugates (1 mg/mL) was added into the luer inlet port 1 of the microfluidic chips and then immediately frozen at a -80 $^{\circ}\text{C}$ refrigerator for half an hour and vacuum freeze-dried for 8 h. After freeze-drying, the chips were stored at room temperature in an airtight plastic bag filled with a silica bead desiccant. Figure 2a shows the formation of the sandwich immunoassay and colorimetric formation. For test procedures, as shown in Figure 2b, first, the chip was put on the magnet, 50 μL (3 drops) of standard N protein solution or the sample was added into the luer inlet port 1 and incubated for 30 min, and the freeze-dried Au@Pt NPs-mAbs conjugates and MB-mAbs conjugates were reacted with the N protein and formed a sandwich structure. Second, 100 μL (6 drops) of wash buffer was added into the luer inlet port 2, 100 μL (6 drops) of one-step TMB substrate solution was added into the luer inlet port 3, the absorbent paper was put into the luer outlet port; then, the T-type silicone rubber plug was put in all three inlets, and the plug of inlet 1 to the bottom was pressed. Through the pressing of the plug, the sample mixture passed the channel, and MB-mAbs conjugates or Au@Pt NPs-mAbs-N protein-MB-antibody sandwich structures were captured by a magnet into the chamber while unreacted Au@Pt NPs-mAbs conjugates and excess liquid were sucked away by absorbent paper. Third, the plug of inlet 2 to the bottom was pressed, and then, the magnet and absorbent paper were removed. The captured MB-mAbs conjugates or Au@Pt NPs-mAbs-N protein-MB-mAbs sandwich structures were washed by wash buffer, while nonspecific adsorbed Au@Pt NPs-mAbs conjugates and excess liquid were sucked away by absorbent paper. Finally, the plug of inlet 3 to the bottom was pressed, and the solution was incubated for 10 min. The TMB substrate solution flushed the MB complex in the chamber into the luer outlet port to react with the captured Au@Pt NPs and develop a color. The developed colors were observed and judged with the naked eyes or transferred to a microwell plate, and the absorbances at 630 nm were measured using a microplate reader.

RESULTS AND DISCUSSION

Characterization of Au@Pt NPs. The Au@Pt NPs were prepared with a controlled size and monodispersed by

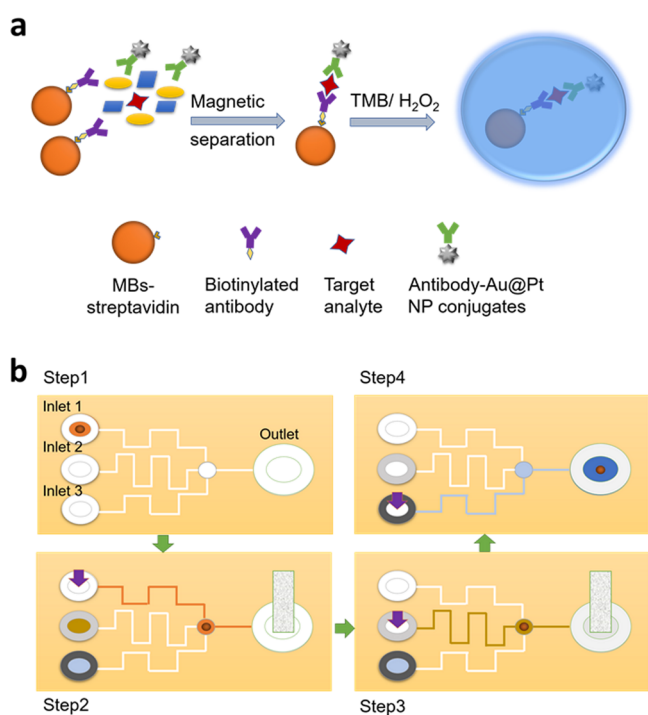


Figure 2. Schematic representation of COVID-19 detection. (a) Principle of the colorimetric formation of the sandwich immunoassay. (b) Illustration of the microfluidic chip immunoassay test procedure. Step 1, put the chip on the magnet, drop the sample into inlet 1, and incubate it for 30 min. Step 2, drop the wash buffer into inlet 2, drop the TMB substrate into inlet 3, put the absorbent paper into the outlet, put the T-type silicone rubber plug in all three inlets, and press the plug of inlet 1 to the bottom. Step 3, press the plug of inlet 2 to the bottom and then remove the magnet and absorbent paper. Step 4, press the plug of inlet 3 to the bottom, incubate for 10 min.

changing the AuNP seed concentration, as shown in Figure 3a,b; the TEM images and dynamic light scattering analysis show that the concentration of AuNP seeds has a significant influence on the Au@Pt NP size. The increased Au NP seed concentration makes the synthesized nanoparticles smaller. Au@Pt NP sizes ranging from 35 to 125 nm were synthesized. Figure S1a,b shows the TEM images of Au NP seeds and Pt NPs prepared without Au NP seeds. The average TEM size of Au NPs is 14.2 nm. The addition of Au NP seeds may control the size of nanoparticles and make the particle size more uniform. Figure S2 shows the high-resolution TEM images and EDS mapping images of a single Au@Pt NP formed from 0.8 nM Au NP seeds; the magnified image shows the lattice fringes of platinum and the elemental mappings indicate a core-shell structure. Figure S3 shows the UV/Vis spectra of Au NP seeds and Au@Pt NPs formed from 0.8 nM Au NP seeds. The surface properties of the Au@Pt NPs were measured by X-ray photoelectron spectroscopy (XPS). As shown in Figure 3c, Pt 4d and 4f peaks were clearly observed, while Au signals were not noticeable. The high-resolution XPS spectra (Figure 3d) indicated that Pt on the surface of Au@Pt NPs was mainly in the form of Pt⁰.

Evaluation of Au@Pt NP Activity. The stability of the peroxidase-like activity of Au@Pt NPs in acidic-to-alkaline pH environments was evaluated. Au@Pt NPs were dispersed in water with different pHs (pH 1–13, adjusted by HCl or NaOH) for up to 30 min and 24 h at room temperature, and the catalytic activity was measured by the addition of TMB

substrate solution and measurement of 630 nm absorbance. Au@Pt NPs (10 pM) reacted with the TMB substrate quickly and reached a plateau at 8–10 min; meanwhile, the signal with a low concentration (0.2 pM) was noticeable by the naked eyes at 8–10 min (Figure S4). Therefore, 10 min was determined to be the ideal time for TMB substrate reaction. In acidic-to-alkaline pH environments, the catalytic activity of Au@Pt NPs was stable at pH 3–12 with a wide optimum pH range (Figure 4a). The catalytic activity of Au@Pt NPs stored in a 4 °C refrigerator, at room temperature, and in a 37 °C incubator has no significant change up to 5 weeks (Figure 4b). For practical SARS-CoV-2 detection, saliva and serum samples were matrices of the most concern, and Au@Pt NPs–mAbs conjugates were found to retain more than 80% of the initial particle activity in saliva samples, serum samples, and urine samples over a period of 24 h (Figure 4c), far in excess of the expected exposure time in a measurement process. The peroxidase-like catalytic efficiencies of Au@Pt NPs were performed by steady-state kinetic assays. The catalytic constant (K_{cat}) was determined through the plot of the initial reaction velocity against TMB concentration and the double-reciprocal plot (Figure 5). The K_{cat} value of Au@Pt NPs was $1.09 \times 10^8 \text{ s}^{-1}$, which was greater than those of Fe₃O₄ NPs, Pt NPs, Ni-Pt NPs, Pd-Ir cubes, and HRP (Table S1).^{25,29,31} The synthesized Au@Pt NPs show high catalytic activity and stability in complex environments.

Performance of the Microfluidic Chip Immunoassay.

Au@Pt NPs were used as catalytic labels in the microfluidic chip immunoassay. Au@Pt NP sizes ranging from 35 to 125 nm were modified with an antibody through coordination bonds of sulfur groups. Keeping the Au@Pt NP concentrations constant, the differently sized Au@Pt NPs–mAb conjugates were used for detection of N protein in PBS with concentrations of 10 and 100 pg/mL. The result of signal intensity variation with particle size is shown in Figure 6a. Larger Au@Pt NPs have an increased surface area available for catalytic reactions showing increased signal intensity. However, Au@Pt NP sizes ranging from 95 to 125 nm show very low variation due to a reduction in diffusivity. The Au@Pt NP size of 75 nm shows optimal signal intensity, and optimization of the added L-mAbs amount to Au@Pt NPs is outlined in Supporting Information Figure S5; these Au@Pt NPs–mAbs conjugates were used for further experiments.

We first evaluated the duration of the microfluidic chip immunoassay. Either Au@Pt NPs–mAbs conjugates (10 μL, 500 pM) or MB–mAbs conjugates (10 μL, 1 mg/mL) were added into a microwell plate and freeze-dried. N protein (50 μL) in PBS with concentrations of 10 and 100 pg/mL was added in a microwell plate; after incubation varying from 5 to 60 min, the absorbance at 630 nm was measured every 5 min for a certain incubation time with magnetic separation and addition of TMB substrate solution. Figure 6b shows that the absorbance intensity dramatically increased from 5 to 40 min, but this increase was attenuated as the incubation time was extended further, and the intensity signal ultimately reached a plateau. N protein with concentrations of 10 and 100 pg/mL both can be detected after incubation for 5 min. To obtain more colors and stable results, the incubation time was optimized for 30 min.

Detection by the Microfluidic Chip Immunoassay. In order to identify the sensitivity of the microfluidic chip immunoassay, the N protein standard samples were evaluated. The tested standard samples were observed and judged with

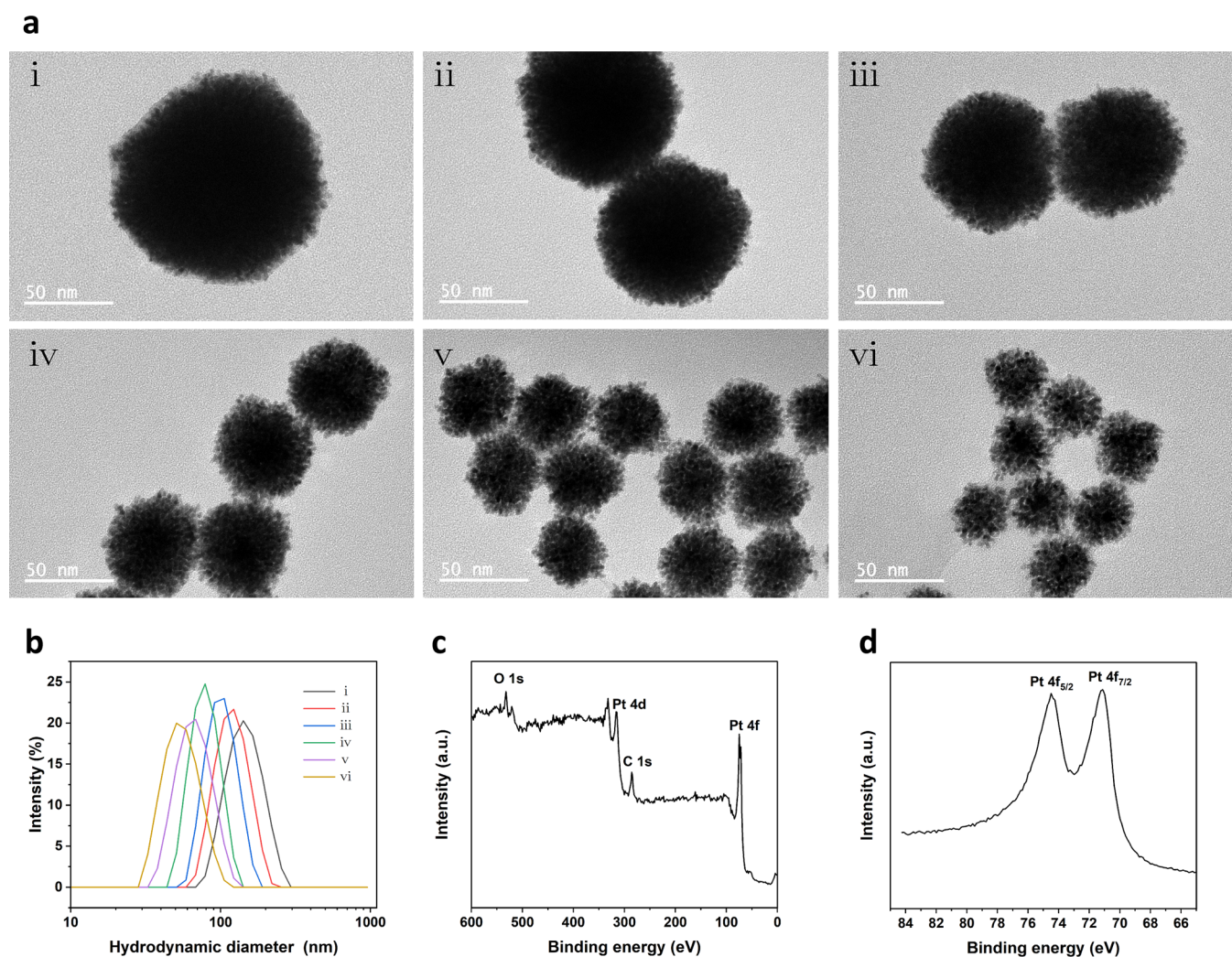


Figure 3. (a) TEM images of Au@Pt NPs synthesized in the presence of different Au NP seed concentrations: (i) 0.2, (ii) 0.4, (iii) 0.8, (iv) 1.6, (v) 3.2, and (vi) 6.4 nM seeds. (b) Intensity distribution of the hydrodynamic diameter of Au@Pt NPs synthesized in the presence of different Au NP seed concentrations measured by DLS. (i) 0.2, (ii) 0.4, (iii) 0.8, (iv) 1.6, (v) 3.2, and (vi) 6.4 nM seeds. (c) XPS spectra of the Au@Pt NPs and (d) high-resolution XPS spectra of the Pt 4f region shown in (c).

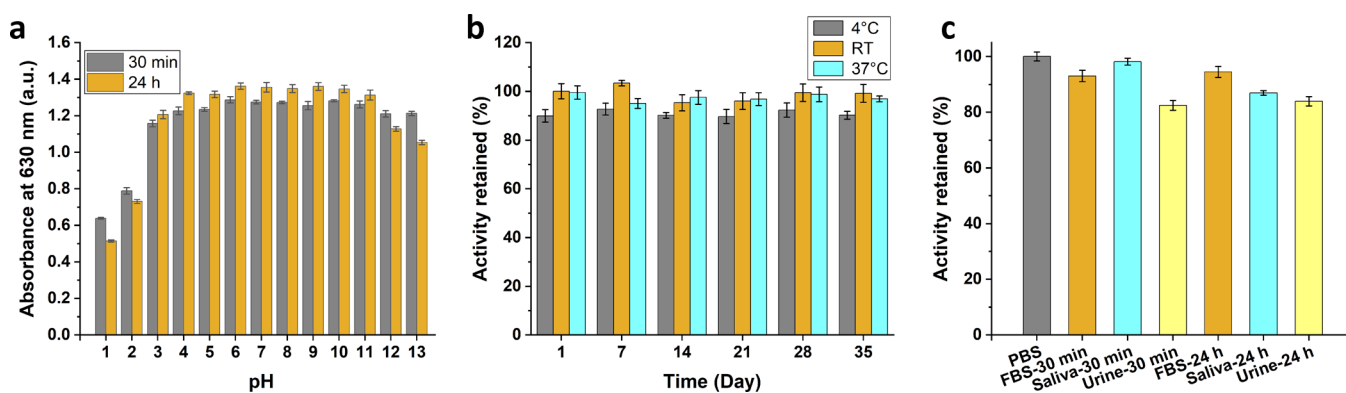


Figure 4. (a) Catalytic activity of Au@Pt NPs incubated in different pH environments up to 24 h. (b) Change of catalytic activity of Au@Pt NPs as a function of storage time. (c) Change of catalytic activity of Au@Pt NPs-mAbs incubated in different sample environments up to 24 h. All data are averaged from three independent measurements, and error bars indicate the standard deviation.

the naked eyes and then measured at 630 nm absorbance in a microwell plate; normal color vision readily discerns the difference in color intensity between the limit concentration and the negative control. The color intensity in the luer outlet port decreased significantly with decreasing sample concen-

tration (Figure 7a). The color intensity measured at 630 nm absorbance represents the concentration of samples at the range of 0.1–1000 pg/mL for N proteins, which is particularly noticeable. The test limit concentration of N proteins using the microfluidic chip immunoassay is 0.1 pg/mL, which is 100

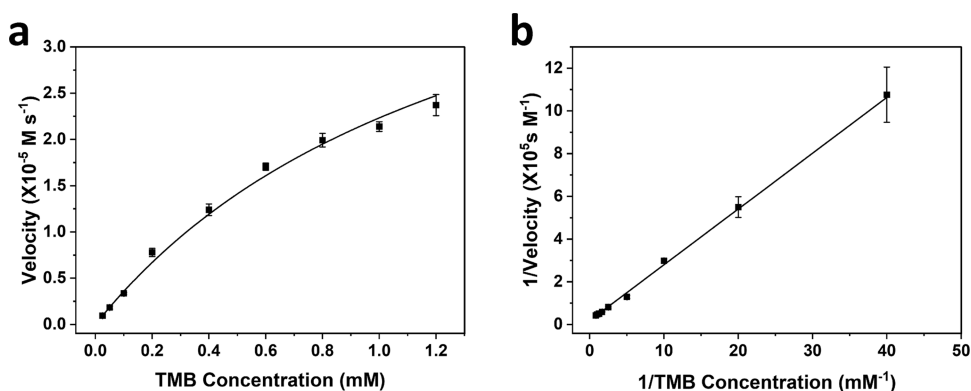


Figure 5. Steady-state kinetic assays of the Au@Pt NPs for the catalytic oxidation of TMB by H_2O_2 . (a) Plot of initial reaction velocity against TMB concentration. (b) Double-reciprocal plot generated from (a), with which the catalytic constant (K_{cat}) was determined. All data are averaged from three independent measurements, and error bars indicate the standard deviations.

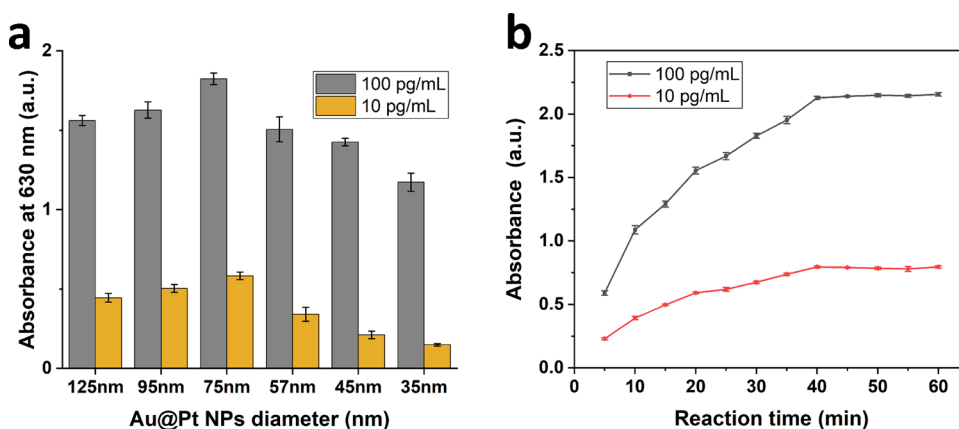


Figure 6. (a) Measurement of 630 nm absorbance for antibody-modified Au@Pt NPs varying in size from ca. 35 to 125 nm (average size by TEM) for detection of 10 and 100 pg/mL N protein in PBS for 10 min after addition of TMB substrate solution. (b) Measurement of 630 nm absorbance for incubation times varying from ca. 5 to 60 min for detection of 10 and 100 pg/mL N protein in PBS for 10 min after addition of TMB substrate solution. Error bars indicate the standard deviation from three independent experiments.

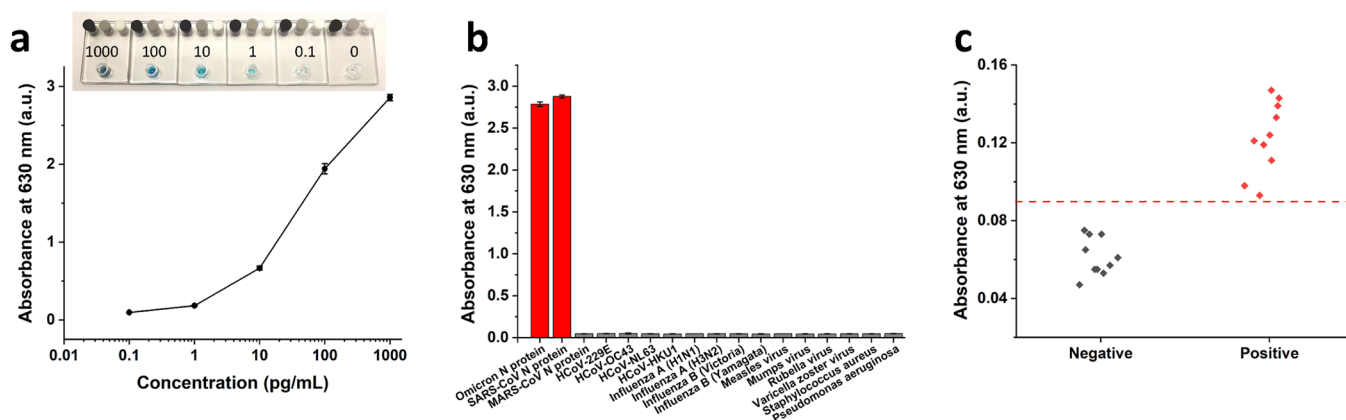


Figure 7. Analytical performance of the microfluidic chip immunoassay: (a) images of the microfluidic chip immunoassay and absorbance intensity obtained at different N protein concentrations ranging from 0.1 to 1000 pg/mL. (b) Cross reaction between several common coronaviruses and pathogens. (c) Throat swab sample collection test. Error bars represent standard deviation from three independent experiments.

times lower compared to conventional Au NP-based LFAs (Figure S6). Moreover, through the absorbance intensity obtained at different N protein concentrations and the negative sample, the cutoff value can be set at 0.9, which is noticeable by the naked eyes and two times the absorbance intensity of the negative sample.

Specificity of the Microfluidic Chip Immunoassay.

The specificity of this microfluidic chip was evaluated using different pathogens, which included SARS-CoV-2 N protein (B.1.1.529 BA.1 strain, omicron), SARS-CoV N protein, MERS-CoV N protein, and common coronavirus strains (HCoV-229E, HCoV-OC43, HCoV-NL63, and HCoV-HKU1), influenza A (H1N1 strain and H3N2 strain),

influenza B (Victoria strain and Yamagata strain), measles virus, mumps virus, rubella virus, varicella zoster virus, *Staphylococcus aureus*, and *Pseudomonas aeruginosa*. As displayed in Figure 7b, SARS-CoV-2 N protein (B.1.1.529 BA.1 strain, omicron) and SARS-CoV N protein yielded positive results, while the other pathogens tested negative. This result demonstrated that the microfluidic chip immunoassay does not cross react with common coronavirus strains and other tested pathogens.

N Protein Detection in Practical Matrices. For practical SARS-CoV-2 detection, throat swab is the mainstream sample collection tool in SARS-CoV-2 screening and diagnosis; thus, the throat swab collection samples can be used to evaluate the performance of this microfluidic chip immunoassay. Ten throat swabs were collected from healthy volunteers, all samples were mixed with virus split solution (containing 0.5 wt % NP 40, 0.2 wt % Tween 20, and 0.2 wt % LNAC in 20 mM PBS, pH 7.4) at a volume of 600 μ L and incubated for 1 min at room temperature, and then, each sample was divided into two groups, where one was for the negative group and the other for the positive group was constructed by spiking N protein into the same samples with a little upper limit of concentration of 0.2 pg/mL. In Figure 7c, the measured result shows the sensitive recognition of trace N protein in throat swab samples by the microfluidic chips. Therefore, this microfluidic chip immunoassay has promising performance in throat swab sample collection modes.

SARS-CoV-2 N protein concentrations were proportional to viral loads.³² The kinetics of serum SARS-CoV-2 N protein showed a median concentration of 1 pg/mL in cases that were asymptomatic at the time of sample collection and dramatically increased from 18 pg/mL on day 1 to 116 pg/mL on day 2 and reached a peak in a week following symptom onset.⁹ The N protein shows high diagnostic sensitivity and specificity during the first week of symptom onset.⁵ The ultralow limit concentration of this microfluidic chip immunoassay (0.1 pg/mL) is expected to perform better in screening of COVID-19. A series of microfluidic chip immunoassays for the detection of SARS-CoV-2 proteins were reported previously (Table S2). In comparison to the electrochemical/chemiluminescent detection method, the colorimetric microfluidic immunoassay proposed in this study provides a lower LOD with comparable detection time.^{12,17,22} The graphene-based biosensors have demonstrated a very low LOD (1 fg/mL) with specific device readout and provided a competitive solution for SARS-CoV-2 screening and diagnosis.^{19–21} Compared with the conventional equipment to operate microfluidic chips with gas pressure sources and a liquid flow system,²⁷ this microfluidic chip immunoassay just uses a T-type silicone rubber plug; therefore, decreasing the complexity of the device is convenient for personal operation. The manufacture of PDMS chips relies on manual operation and is difficult for large-scale production. However, PMMA chips can be mass-produced by the injection molding method at a very low cost. The cost of this microfluidic chip immunoassay kit is \$1.227 per test (Table S3).

CONCLUSIONS

In this study, we have developed a simple and cost-effective Au@Pt NP-based microfluidic chip immunoassay platform for ultrasensitive colorimetric detection of SARS-CoV-2 N protein. This microfluidic chip immunoassay could detect SARS-CoV-2 N protein as low as 0.1 pg/mL within 40 min.

The microfluidic chip immunoassay platform demonstrated a high sensitivity and easy operation and readout without equipment and has the potential to be extended for diagnostics of other viruses and biomarkers by switching detecting antibodies. Multiplex microfluidic platforms for simultaneous and multiple detection of respiratory viruses such as SARS-CoV-2, influenza, respiratory syncytial virus, parainfluenza virus, and adenovirus can be developed in the future. The excellent performance of the developed microfluidic chip immunoassay is attributed to the high catalytic activity of Au@Pt NPs. Au@Pt NPs have the advantages of good stability, low cost, a simple preparation process, and an easy combination with the microfluidic chip immunoassay, which opens up possibilities for future pathogen surveillance and in-home healthcare.

ASSOCIATED CONTENT

Supporting Information

The Supporting Information is available free of charge at <https://pubs.acs.org/doi/10.1021/acsbiomaterials.2c00600>.

Additional experimental details, TEM images of Au NPs and Pt NPs, high-resolution TEM image and EDS mapping image of individual Au@Pt NPs, UV/Vis spectra of Au NP seeds and Au@Pt NPs, time curve of Au@Pt NPs with different concentrations after addition of the TMB substrate, plot of positive intensity at 10 pg/mL to the background ratio against varying antibody amounts conjugated with Au@Pt NPs, representative photographs taken from the AuNP LFAs of N protein standards using the same antibodies, comparison of the kinetic parameters of 75 nm Au@Pt NPs and other peroxidase mimics toward the oxidation of TMB by H₂O₂, comparison of the microfluidic chip immunoassays for the detection of SARS-CoV-2 proteins, and cost estimation of materials in the microfluidic chip immunoassay kit (PDF)

AUTHOR INFORMATION

Corresponding Author

Lan Ma – Institute of Biopharmaceutical and Health Engineering, Tsinghua Shenzhen International Graduate School, Tsinghua-Berkeley Shenzhen Institute, and State Key Laboratory of Chemical Oncogenomics, Tsinghua Shenzhen International Graduate School, Tsinghua University, Shenzhen 518055, China; Institute of Biomedical Health Technology and Engineering, Shenzhen Bay Laboratory, Shenzhen 518055, China; orcid.org/0000-0002-6610-5871; Phone: +86-755-26033033; Email: malan@sz.tsinghua.edu.cn

Authors

Feng Wu – School of Life Sciences, Tsinghua University, Beijing 100084, China; Institute of Biopharmaceutical and Health Engineering, Tsinghua Shenzhen International Graduate School, Tsinghua University, Shenzhen 518055, China; orcid.org/0000-0003-2232-4797

Mao Mao – School of Life Sciences, Tsinghua University, Beijing 100084, China; Institute of Biopharmaceutical and Health Engineering, Tsinghua Shenzhen International Graduate School, Tsinghua University, Shenzhen 518055, China

Liangyu Cai – School of Life Sciences, Tsinghua University, Beijing 100084, China; Institute of Biopharmaceutical and Health Engineering, Tsinghua Shenzhen International Graduate School, Tsinghua University, Shenzhen 518055, China

Qianyu Lin – Tsinghua-Berkeley Shenzhen Institute, Tsinghua University, Shenzhen 518055, China

Xuejiao Guan – School of Life Sciences, Tsinghua University, Beijing 100084, China; Institute of Biopharmaceutical and Health Engineering, Tsinghua Shenzhen International Graduate School, Tsinghua University, Shenzhen 518055, China

Xueying Shi – Institute of Biopharmaceutical and Health Engineering, Tsinghua Shenzhen International Graduate School, Tsinghua University, Shenzhen 518055, China;

orcid.org/0000-0003-0384-560X

Complete contact information is available at:

<https://pubs.acs.org/10.1021/acsbmaterials.2c00600>

Author Contributions

The manuscript was written through contributions of all authors. All authors have given approval to the final version of the manuscript.

Notes

The authors declare no competing financial interest.

ACKNOWLEDGMENTS

This work was supported by Shenzhen Science and Technology research and development funds (JCYJ20200109143018683), the State Key Laboratory of Chemical Oncogenomics, and the Institute of Biomedical Health Technology and Engineering at the Shenzhen Bay Laboratory.

REFERENCES

- (1) Araf, Y.; Akter, F.; Tang, Y.; Fatemi, R.; Parvez, M. S. A.; Zheng, C.; Hossain, M. G. Omicron variant of SARS-CoV-2: Genomics, transmissibility, and responses to current COVID-19 vaccines. *J. Med. Virol.* **2022**, *94*, 1825–1832.
- (2) Broughton, J. P.; Deng, X.; Yu, G.; Fasching, C. L.; Servellita, V.; Singh, J.; Miao, X.; Streithorst, J. A.; Granados, A.; Sotomayor-Gonzalez, A.; et al. CRISPR–Cas12-based detection of SARS-CoV-2. *Nat. Biotechnol.* **2020**, *38*, 870–874.
- (3) Yelagandula, R.; Bykov, A.; Vogt, A.; Heinen, R.; Özkan, E.; Strobl, M. M.; Baar, J. C.; Uzunova, K.; Hajdusits, B.; Kordic, D.; et al. Multiplexed detection of SARS-CoV-2 and other respiratory infections in high throughput by SARSeq. *Nat. Commun.* **2021**, *12*, 3132.
- (4) Ding, X.; Yin, K.; Li, Z.; Lalla, R. V.; Ballesteros, E.; Sfeir, M. M.; Liu, C. Ultrasensitive and visual detection of SARS-CoV-2 using all-in-one dual CRISPR-Cas12a assay. *Nat. Commun.* **2020**, *11*, 4711.
- (5) Corman, V. M.; Landt, O.; Kaiser, M.; Molenkamp, R.; Meijer, A.; Chu, D. K. W.; Bleicker, T.; Brünink, S.; Schneider, J.; Schmidt, M. L. Detection of 2019 novel coronavirus (2019-nCoV) by real-time RT-PCR. *Eurosurveillance* **2020**, *25*, 2000045.
- (6) Smith, D. R. M.; Duval, A.; Zahar, J. R.; Hendrickx, N.; Jean, K.; Jijón, S.; Oodally, A.; Shirreff, G.; Tamandjou, C.; Opatowski, L.; et al. Rapid antigen testing as a reactive response to surges in nosocomial SARS-CoV-2 outbreak risk. *Nat. Commun.* **2022**, *13*, 236.
- (7) Diao, B.; Wen, K.; Zhang, J.; Chen, J.; Han, C.; Chen, Y.; Wang, S.; Deng, G.; Zhou, H.; Wu, Y. Accuracy of a nucleocapsid protein antigen rapid test in the diagnosis of SARS-CoV-2 infection. *Clin. Microbiol. Infection* **2021**, *27*, 289.e281–289.e284.
- (8) Liu, D.; Wu, F.; Cen, Y.; Ye, L.; Shi, X.; Huang, Y.; Fang, S.; Ma, L. Comparative research on nucleocapsid and spike glycoprotein as the rapid immunodetection targets of COVID-19 and establishment of immunoassay strips. *Mol. Immunol.* **2021**, *131*, 6–12.
- (9) Zhang, Y.; Ong, C. M.; Yun, C.; Mo, W.; Whitman, J. D.; Lynch, K. L.; Wu, A. H. B. Diagnostic Value of Nucleocapsid Protein in Blood for SARS-CoV-2 Infection. *Clin. Chem.* **2021**, *68*, 240–248.
- (10) Kim, S.; Ryu, H.; Tai, S.; Pedowitz, M.; Rzaia, J. R.; Pennachio, D. J.; Hajzuz, J. R.; Milton, D. K.; Myers-Ward, R.; Daniels, K. M. Real-time ultra-sensitive detection of SARS-CoV-2 by quasi-free-standing epitaxial graphene-based biosensor. *Biosens. Bioelectron.* **2022**, *197*, No. 113803.
- (11) Raziq, A.; Kidakova, A.; Boroznjak, R.; Reut, J.; Öpik, A.; Syritski, V. Development of a portable MIP-based electrochemical sensor for detection of SARS-CoV-2 antigen. *Biosens. Bioelectron.* **2021**, *178*, No. 113029.
- (12) Li, J.; Lillehoj, P. B. Microfluidic Magneto Immunosensor for Rapid, High Sensitivity Measurements of SARS-CoV-2 Nucleocapsid Protein in Serum. *ACS Sensors* **2021**, *6*, 1270–1278.
- (13) Ge, C.; Feng, J.; Zhang, J.; Hu, K.; Wang, D.; Zha, L.; Hu, X.; Li, R. Aptamer/antibody sandwich method for digital detection of SARS-CoV2 nucleocapsid protein. *Talanta* **2022**, *236*, No. 122847.
- (14) Sadique, M. A.; Yadav, S.; Ranjan, P.; Khan, R.; Khan, F.; Kumar, A.; Biswas, D. Highly Sensitive Electrochemical Immunosensor Platforms for Dual Detection of SARS-CoV-2 Antigen and Antibody based on Gold Nanoparticle Functionalized Graphene Oxide Nanocomposites. *ACS Appl. Bio Mater.* **2022**, *5*, 2421–2430.
- (15) Singhal, A.; Parihar, A.; Kumar, N.; Khan, R. High throughput molecularly imprinted polymers based electrochemical nanosensors for point-of-care diagnostics of COVID-19. *Mater. Lett.* **2022**, *306*, No. 130898.
- (16) Abubakar Sadique, M.; Yadav, S.; Ranjan, P.; Akram Khan, M.; Kumar, A.; Khan, R. Rapid detection of SARS-CoV-2 using graphene-based IoT integrated advanced electrochemical biosensor. *Mater. Lett.* **2021**, *305*, No. 130824.
- (17) Tan, X.; Krel, M.; Dolgov, E.; Park, S.; Li, X.; Wu, W.; Sun, Y.-L.; Zhang, J.; Khaing Oo, M. K.; Perlin, D. S.; et al. Rapid and quantitative detection of SARS-CoV-2 specific IgG for convalescent serum evaluation. *Biosens. Bioelectron.* **2020**, *169*, No. 112572.
- (18) Wang, C.; Wang, C.; Qiu, J.; Gao, J.; Liu, H.; Zhang, Y.; Han, L. Ultrasensitive, high-throughput, and rapid simultaneous detection of SARS-CoV-2 antigens and IgG/IgM antibodies within 10 min through an immunoassay biochip. *Microchim. Acta* **2021**, *188*, 262.
- (19) Seo, G.; Lee, G.; Kim, M. J.; Baek, S.-H.; Choi, M.; Ku, K. B.; Lee, C.-S.; Jun, S.; Park, D.; Kim, H. G.; et al. Rapid Detection of COVID-19 Causative Virus (SARS-CoV-2) in Human Nasopharyngeal Swab Specimens Using Field-Effect Transistor-Based Biosensor. *ACS Nano* **2020**, *14*, 5135–5142.
- (20) Li, Y.; Peng, Z.; Holl, N. J.; Hassan, M. R.; Pappas, J. M.; Wei, C.; Izadi, O. H.; Wang, Y.; Dong, X.; Wang, C.; et al. MXene–Graphene Field-Effect Transistor Sensing of Influenza Virus and SARS-CoV-2. *ACS Omega* **2021**, *6*, 6643–6653.
- (21) Sharma, P. K.; Kim, E.-S.; Mishra, S.; Ganbold, E.; Seong, R.-S.; Kaushik, A. K.; Kim, N.-Y. Ultrasensitive and Reusable Graphene Oxide-Modified Double-Interdigitated Capacitive (DIDC) Sensing Chip for Detecting SARS-CoV-2. *ACS Sensors* **2021**, *6*, 3468–3476.
- (22) Xu, J.; Suo, W.; Goulev, Y.; Sun, L.; Kerr, L.; Paulsson, J.; Zhang, Y.; Lao, T. Handheld Microfluidic Filtration Platform Enables Rapid, Low-Cost, and Robust Self-Testing of SARS-CoV-2 Virus. *Small* **2021**, *17*, e2104009.
- (23) Gao, Z.; Ye, H.; Tang, D.; Tao, J.; Habibi, S.; Minerick, A.; Tang, D.; Xia, X. Platinum-Decorated Gold Nanoparticles with Dual Functionalities for Ultrasensitive Colorimetric in Vitro Diagnostics. *Nano Lett.* **2017**, *17*, 5572–5579.
- (24) Loynachan, C. N.; Thomas, M. R.; Gray, E. R.; Richards, D. A.; Kim, J.; Miller, B. S.; Brookes, J. C.; Agarwal, S.; Chudasama, V.; McKendry, R. A. Platinum Nanocatalyst Amplification: Redefining the Gold Standard for Lateral Flow Immunoassays with Ultrabroad Dynamic Range. *ACS Nano* **2018**, *12*, 279–288.

- (25) Xi, Z.; Wei, K.; Wang, Q.; Kim, M. J.; Sun, S.; Fung, V.; Xia, X. Nickel–Platinum Nanoparticles as Peroxidase Mimics with a Record High Catalytic Efficiency. *J. Am. Chem. Soc.* **2021**, *143*, 2660–2664.
- (26) Wrasman, C. J.; Boubnov, A.; Riscoe, A. R.; Hoffman, A. S.; Bare, S. R.; Cargnello, M. Synthesis of Colloidal Pd/Au Dilute Alloy Nanocrystals and Their Potential for Selective Catalytic Oxidations. *J. Am. Chem. Soc.* **2018**, *140*, 12930–12939.
- (27) Zheng, L.; Cai, G.; Qi, W.; Wang, S.; Wang, M.; Lin, J. Optical Biosensor for Rapid Detection of *Salmonella typhimurium* Based on Porous Gold@Platinum Nanocatalysts and a 3D Fluidic Chip. *ACS Sensors* **2020**, *5*, 65–72.
- (28) Frens, G. Controlled Nucleation for the Regulation of the Particle Size in Monodisperse Gold Suspensions. *Nat. Phys. Sci.* **1973**, *241*, 20–22.
- (29) Jiang, B.; Duan, D.; Gao, L.; Zhou, M.; Fan, K.; Tang, Y.; Xi, J.; Bi, Y.; Tong, Z.; Gao, G. F.; et al. Standardized assays for determining the catalytic activity and kinetics of peroxidase-like nanozymes. *Nat. Protoc.* **2018**, *13*, 1506–1520.
- (30) Tian, H.; Zhao, W.; Liu, X.; Liu, C.; Peng, N. Integrated Single Microbead-Arrayed μ -Fluidic Platform for the Automated Detection of Multiplexed Biomarkers. *ACS Sens.* **2020**, *5*, 798–806.
- (31) Xia, X.; Zhang, J.; Lu, N.; Kim, M. J.; Ghale, K.; Xu, Y.; McKenzie, E.; Liu, J.; Ye, H. Pd–Ir Core–Shell Nanocubes: A Type of Highly Efficient and Versatile Peroxidase Mimic. *ACS Nano* **2015**, *9*, 9994–10004.
- (32) Mayanskiy, N.; Brzhozovskaya, E.; Fedorova, N.; Lebedin, Y. Parallel detection of SARS-CoV-2 RNA and nucleocapsid antigen in nasopharyngeal specimens from a COVID-19 patient screening cohort. *Int. J. Infect. Diseases* **2021**, *108*, 330–332.